3D printing multifunctional fluorinated nanocomposites: Tuning electroactivity, rheology and chemical reactivity

Journal:	*Journal of Materials Chemistry A*
Manuscript ID	TA-ART-01-2018-000127.R1
Article Type:	Paper
Date Submitted by the Author:	04-Apr-2018
Complete List of Authors:	Bencomo, Jose; University of Colorado Colorado Springs, Mechanical and Aerospace Engineering Iacono, Scott; United States Air Force Academy, Department of Chemistry McCollum, Jena; University of Colorado at Colorado Springs, Mechanical and Aerospace Engineering

Journal Name

ARTICLE

3D printing multifunctional fluorinated nanocomposites: Tuning electroactivity, rheology and chemical reactivity

Received 00th January 20xx,
Accepted 00th January 20xx

DOI: 10.1039/x0xx00000x

www.rsc.org/

Jose A. Bencomo[a], Scott T. Iacono[b], and Jena McCollum*[a]

Poly(methyl methacrylate) (PMMA) was added to aluminum/poly(vinylidene fluoride) (Al/PVDF) energetic blends to enhance melt flow rate and adhesion in a fused deposition modeling (FDM) manufacturing scenario. Composites were successfully printed with up to 30 wt% nano-scale Al after PMMA addition. Melt flow rate increased with increasing PMMA content. This resulted in a partially fluorinated binder that can facilitate high solids loadings and can be easily printed with a standard FDM 3D printer. PMMA addition promoted nucleation of the electroactive β-phase PVDF, which suggests the potential to print piezoelectric, energetic composites. Thermal stability was assessed using differential scanning calorimetry and thermogravimetric analysis. Results verified that composite stability decreased with increasing PMMA and Al content, however, decomposition onset temperatures for all concentrations remained well above printing temperatures. Burn rates at higher Al loadings (e.g., fuel rich) showed a decreasing trend. Analysis of post burn soot revealed α-AlF_3 and amorphous carbon char as the primary reaction products. Combustion performance results indicate that although PMMA may serve as a heat sink, the reaction between Al and PVDF was not significantly affected by PMMA addition. These findings indicate that by changing PMMA concentrations, rheology, piezoelectric content, thermal properties and combustion performance can be altered to suit specific needs.

Introduction

In recent years, additive manufacturing has expanded to include traditional prototyping technologies such as fused deposition modeling (FDM). The limitation in bridging the gap between prototyping and manufacturing is the limited access to specialty feedstocks. There is also a need to establish effective processing techniques for nanoscale composites that are applicable to macroscopic processing.[1] One application that would benefit from this manufacturing method is the development of structural energetics. Although some groups have employed solvent-based techniques to produce structural energetics, little has been done to melt-process these blends. This limitation is caused by large viscosity increases with high loadings of metallic fuel particles, which makes processing a challenge.[2–4] These viscosity limitations increase with the addition of nanoscale particulate.[5] PVDF/PMMA blends have been extensively studied due to their optical performance, piezoelectric properties, chemical resistance, mechanical strength, and weatherability.[6–8] Introducing PMMA into the PVDF matrix improves PVDF processability.[9]

These additive manufacturing techniques have the potential to produce multifunctional materials (e.g., piezoelectric energetic composites). The β-phase PVDF polymorph exhibits strong piezoelectric properties and is most commonly obtained through mechanical stretching of the α-phase and by the addition of nucleating fillers (e.g., PMMA[10]). The addition of PMMA persuades the formation of β-phase PVDF by increasing the β-nucleation temperature and by the increased amount of trans-trans conformations of PVDF.[11,12] This interaction may be useful in the development of piezoelectric binders to tune ignition sensitivity of energetic composites. PMMA is completely miscible in PVDF for PVDF concentrations less than 50 wt%.[13] As previously found by Sengupta et al.[14] and Hahn et al.,[15] when PVDF concentrations exceed 50 wt% and temperatures are between the glass transition (T_g) and the melting point (T_m), the blend exhibits two phases; a PVDF crystalline phase and a PVDF/PMMA amorphous phase. Good miscibility between PVDF and PMMA provides a suitable foundation for the introduction of nanoparticles (e.g., nAl).

Aluminum is used extensively as a fuel in energy generating applications (e.g., solid rocket propellants) due to its highly desirable combustion characteristics.[16] In solid rocket propellants, aluminum particles range between 5 and 60 µm.[17] As microscale aluminum (µAl) burns in a PVDF binder, the propagation of energy is limited by the inter-particle distance, that is, PVDF acts as a thermal barrier.[18] Specific surface area significantly increases when particle diameters reach the

---

[a] *Department of Mechanical and Aerospace Engineering, University of Colorado Colorado Springs, Colorado Springs, Colorado (USA)*

[b] *Department of Chemistry and Chemistry Research Center, United States Air Force Academy, Colorado Springs, Colorado (USA)*

* Corresponding Author

Electronic Supplementary Information (ESI) available: [details of any supplementary information available should be included here]. See DOI: 10.1039/x0xx00000x nanoscale, which increases linear burn rates by 100% or more.[19–21] However, with decreasing particle sizes, the mass fraction of the oxide layer increases. This reduces the energy density of aluminum.[22] The use of a fluoropolymer as an oxidizer or reactive binder for aluminum fuel improves the oxidation efficiency due to the fluorine atoms reacting with the aluminium or alumina shell producing AlF_3.[18] Crouse et al. observed optimum reactivity in stoichiometric aluminized fluorinated acrylate (AlFA) blends.[21] Stoichiometric fluoropolymer/nAl composites experience optimized reaction rates due to complete fluorination, producing the most energetic response.[23] By varying the PMMA content in PVDF/Al blends, stoichiometry can be altered, thus, combustion properties can be changed to suit specific needs. Fluoropolymers also have the potential to introduce useful mechanical properties due to the continuous phase at the particle-polymer interface.[12,21] Enhanced mechanical properties positively alter the melt flow rate resulting in a material that can be processed using established macroscopic techniques. In this study, the rheological and structural effects of PMMA and nAl in PVDF are analyzed by melt flow rate (MFR), Fourier transform infrared (FTIR) spectroscopy, differential scanning calorimetry (DSC), thermogravimetric analysis (TGA), X-ray diffraction (XRD), and combustion performance. Furthermore, energetic nanocomposite formulations as melt-processed filament were 3D printed and their optimized energetic output was evaluated. This work expands on new materials chemistry in the emerging area of structural energetics.

Experimental

Materials

Poly(vinylidene fluoride) (PVDF) powder (Alfa Aesar, Ward Hill, MA) with an average molecular weight of 3.5×10^5 g/mol and poly(methyl methacrylate) (PMMA) beads (Scientific Polymer Products, Inc., Ontario, NY) with an approximate molecular weight of 7.5×10^4 g/mol were used as a binder. Aluminum nanopowder (Novacentrix, Austin, TX) with an average particle size of 80 nm and a specific surface area of 25 m^2/g were used as a fuel. The nanopowder has 75% active aluminum content by mass. All materials were used as received. "PVDFXX-YY" is the nomenclature structure for samples used in this study where "XX" indicates PMMA content and "YY" indicates aluminum content by weight % in PVDF (e.g., 15 wt% PMMA with 30 wt% nAl in PVDF is designated by PVDF15-30).

Sample Preparation

The blends were weighed dry (batches usually contain ca. 7 g of blended materials) and hand mixed for 5 min. The mixture was manually fed into a Thermo Scientific HAAKE Minilab II (Waltham, MA) and compounded at 190 °C and 75 rpm for 5 min. The melt-blended products were then extruded to form filament approximately 2 mm in diameter. Typically, melt extruded filament length was approximately 0.5 m. The filament was used in an Ultimaker 2 (Cambridge, MA) to create the 3D printed specimens. Solidworks 2016 (Waltham, MA) and Cura were used to model the specimens before printing. Printing of the energetic composites was done on a glass plate heated to 60°C through a 0.4 mm nozzle heated to 230°C. The layers were printed with 100% infill density with a layer height of 0.1 mm at 10 mm/s with final dimensions of 5x1x0.2 cm. An initial layer of poly(lactic acid) (PLA) was used to form the brim material to improve adhesion to the glass plate.

Characterization

Melt Flow Index. To assess capillary flow properties of the matrix blends (i.e., no Al loading), melt flow rate (MFR) was obtained using a melt flow indexer from Testing Machines, Inc. (New Castle, DE). Approximately 10 g of each sample was inserted into the heated cylinder at 230°C (i.e., the print nozzle temperature) and allowed to reach a complete molten state, which took approximately ten minutes. The molten polymer was extruded through a tungsten carbide die loaded with 10 kg. An average MFR for each sample was taken from five iterations.

Fourier Transform Infrared Spectroscopy. To assess piezoelectric potential, PVDF crystalline phases were identified using Fourier transform infrared (FTIR) spectroscopy. Absorption spectra were collected using a Thermo Scientific FTIR-ATR Nicolet iS10 (Waltham, MA). A background spectrum was collected before each sample scan. Sample spectra were collected in the range of 600 to 1800 cm^{-1} averaged from 64 scans with a 2 cm^{-1} spectral resolution.

Thermal Analysis. Thermal analysis was performed using a TA Instruments Q600 SDT (i.e., simultaneous differential scanning calorimeter (DSC) and thermogravimetric analyzer (TGA)) (New Castle, DE). Samples were heated at a rate of 5°C/min from 30°C to 700°C under a constant flow of argon (25 mL/min). Samples of approximately 5 mg were placed into an alumina crucible and loaded into the SDT. TGA/DSC info?

Burn Rate. High-speed videos were captured on a Phantom v7.3 high-speed camera (Wayne, NJ) at a sample rate of 4000 fps with an exposure of 10 µs and an extreme dynamic range (EDR) of 5 µs. Samples were attached to a ring stand, enclosed in an acrylic barrier, and ignited with a propane torch. A calibration image was taken prior to the first burn. Flame speeds were then calculated using an image processing code in MATLAB. Since all the high-speed videos used the same reference image, the pixel to cm conversion was hardcoded leaving the video itself as the only input. The created function took advantage of a nearly circular ignition point to locate the beginning of the burn and use it as a reference. The remaining code tracked the flame front by using the embedded edge function along the burn line. Data points were ignored if the points deviated too far from the expected flame front while a running average was calculated.

X-Ray Diffraction. X-ray diffraction measurements were completed by the Bragg-Brentano focusing method on a Rigaku SmartLab X-ray diffractometer (The Woodlands, TX) with a CuKα radiation source and a CuKβ filter at an operating voltage and current of 40 kV and 44 mA, respectively. Measurement profiles were collected from 5° to 70° in continuous scan mode at 3 deg/min with a step width of 0.01° on a θ/2θ scan axis. The post-burn soot was tightly packed into a glass sample holder and loaded into the XRD after optic calibration. Sample alignment was performed prior to each sample data collection.

Results and Discussion

Composite Characterization

PMMA was chosen over other non-fluorinated polymers as a filler in Al/PVDF composites due to the good miscibility properties with PVDF. To determine the influence of PMMA on the processability of the composites, the melt flow index was measured. The melt flow rate was determined using equation 1 where T_t and m_{nom} are the testing conditions (i.e., temperature and load), t_{ref} is the reference time (i.e., 600 s), m is the mass of the extrudate, and t is the cut off interval time (i.e., 10 s).

$$MFR(T_t, m_{nom}) = \frac{t_{ref} \times m}{t} \qquad (1)$$

PVDF and PMMA have an MFR of 2.54 and 15.4 g/10min, respectively. From the data presented in table 1, melt flow rates show a linear relation with respect to PMMA content. This linear relation provides a method to finding an ideal melt flow rate for mixtures of the two virgin polymers. The increase in MFR with increasing PMMA content can be attributed to the miscibility of the system. The increase in MFR indicates that increasing PMMA concentrations will improve processability via FDM. Figure 1 shows a graphical representation of the manufacturing process, the print head on the 3D printer creating the specimens seen in Figures 1c and 1d. It is clear from Figures 1c-d that these composites print well with a standard 3D printer. Figure 1e depicts the combustion of printed specimens. Composites without PMMA addition under the same conditions and settings did not create usable specimens for the study. The addition of PMMA improved the melt flow rate of the composites to facilitate 3D printing. Although increasing PMMA beyond 25 wt% is expected to further increase the melt flow rate, concentrations above 30 wt% increases stoichiometry beyond usability (discussed later in this study) and will not be examined here.

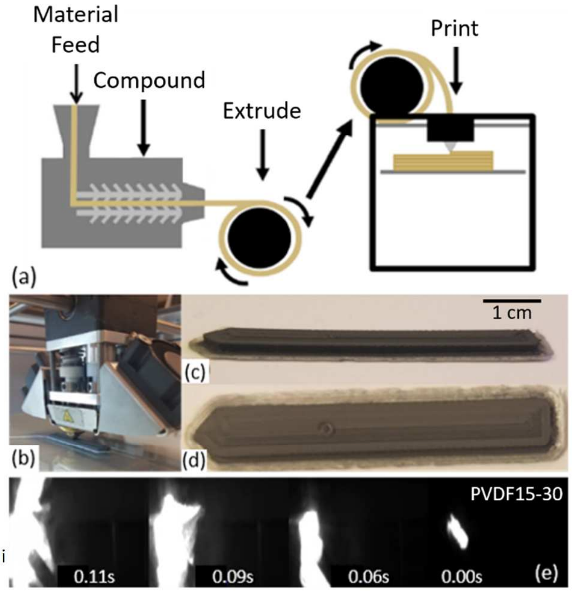

Figure 1 - (a) Graphical representation of manufacturing process (a), Printing the PVDF/PMMA/nAl composites (b), the completed print, side view (c) and top view (d) and burning of reactive composite (e).

Table 1 - Melt flow rates for PVDF composites not loaded with aluminum.

Sample	Melt Flow Rate *[g/10min]*
PVDF0-0 (100% PVDF)	2.544 ± 0.001
PVDF15-0	4.128 ± 0.001
PVDF20-0	4.416 ± 0.001
PVDF25-0	6.288 ± 0.002
PVDF100-0 (100% PMMA)	15.41 ± 0.01

FTIR-ATR was used to determine the structural effects of PMMA on PVDF after melt blending at various loadings. Figure S1 shows the spectra for PVDF, PMMA, and several PVDF/PMMA composites in the range 600 to 1800 cm^{-1} at room temperature. PVDF is known for having five crystalline phases; α, β, γ, δ, and ε.[24,25] The representative peaks of PVDF α- (e.g., 614, 766, 795, 855 and 976 cm^{-1}), β- (e.g., 840 and 1279 cm^{-1}) and γ- (e.g., 776, 812, 833, 840, and 1234 cm^{-1}) phases were used to identify phase composition.[10]

There are two frequency bands in PMMA that are of interest. At 1720 cm^{-1}, the stretching frequency of C=O, and at 990 cm^{-1}, the bending frequency of CH_3—O, are present in PMMA and all blends containing PMMA.[8,26] The band at 1720 cm^{-1} for PMMA is shifted to 1727 cm^{-1}; this shift corresponds to the carbonyl group in PMMA interacting with the CH_2 group in PVDF.[25] Other groups concluded that this interaction assists nucleation of the β-phase PVDF polymorph.[27] Although spectra showed a shoulder around 1234 cm^{-1}, other representative peaks for γ-phase PVDF were not present, indicating that the PVDF crystalline domains primarily consisted of α and β phases.

To determine the β-phase content in the blends, Equation 2 is used, where $F(\beta)$ is the β-phase content, A_α and A_β are the absorbance intensities for α- and β-phase at 762 and 840 cm^{-1}, respectively, and K_α and K_β are the absorption coefficients at the respective wavenumbers, where K_α is 6.1×10^4 cm^2/mol and K_β is 7.7×10^4 cm^2/mol.[10]

$$F(\beta) = \frac{A_\beta}{(K_\beta/K_\alpha)A_\alpha + A_\beta} \cdot 100 \qquad (2)$$

Table 2 - β-phase content in PVDF and PVDF/PMMA blends.

	F(β) [%]		
YY/wt% nAl	0	15	30
PVDF0-YY	38	41	42
PVDF15-YY	54	49	43
PVDF20-YY	56	55	43
PVDF25-YY	58	53	44

The results in Table 2 show an increase in β-phase as the PMMA content increases, which is consistent with the findings of Freire et al..[28] Although β-phase concentration consistently increases with PMMA loading for all nAl concentrations, there is a decreasing trend in β-phase concentration with increasing Al loading. This could presumably be due to the carbonyl group from PMMA interacting with the Al oxide surface instead of the CH_2 group from PVDF. The band at 1727 cm^{-1} confirms the presence of PMMA in the composites. However, in Figures S2a and S2b, this band is shown at a lower wavenumber (1715 cm^{-1}). The shift from 1727 to 1715 cm^{-1} is due to the hydrogen bonding of the carbonyl group with the Al oxide layer with the presence of free Al-OH functionality.[29] This interaction impedes the nucleation of β-phase in the composites with increasing PMMA and Al loadings. The peak at 975 cm^{-1} is disrupted from that of pure PVDF for both 15 and 30 wt% nAl. This could be the interaction between CF dipoles and the strong bond dipoles from Al-O mixing with Al-F. This interaction can facilitate the adhesion at the PVDF-nAl interface, which assists homogenous dispersion of nAl in the PVDF matrix.[30] Peaks corresponding to α- and β-phase are also identified in Figures S2a and S2b.

Thermal Analysis

Figure S3 shows the heat flow and mass loss curves for PVDF, PMMA, and their blends. The melt temperature for pure PVDF is 161.0°C which correlates to the presence of α-phase crystals in PVDF.[25] This was confirmed by FTIR-ATR results shown in Figure S1. As PMMA concentration increases, the melt temperature decreases in all samples regardless of Al loading. This is likely due to an increase in β-phase content as β-phase PVDF experiences a lower melting onset temperature than α-phase.[10] This finding was confirmed with FTIR-ATR (see Table 3).

To assess the impact of PMMA on PVDF crystalline domains, composite crystallinity (X_c) was calculated by using Equation 3 where ΔH_m is the melting enthalpy of the blend (obtained through DSC analysis), ΔH^*_m is the melting enthalpy of 100% crystalline enthalpy (i.e.,104.5 J/g[25,31]), and ϕ is the weight fraction of PVDF.[32]

$$X_c = \frac{\Delta H_m}{\Delta H^*_m \phi} \times 100\% \qquad (3)$$

It is evident from Table 3 that as the PMMA content increases, the melt temperature and the degree of crystallinity decreases. These findings support the results obtained from studies performed by both Gregorio et al. and Freire et al.[13,28].

Crystal growth is described by a driving function (i.e., lamella deposition on the end of a fibril) and a transport function (i.e., delivery of subsequent chains for deposition). This phenomenon and the critical fibril length for an optimized growth rate is highly temperature dependent.[33] The relationship between the driving and transport functions can be tuned by exploring binary polymer blends. In this scenario, crystal growth rate is affected by the smaller concentration of crystallizable polymer at the growth front (i.e., PVDF).[33]

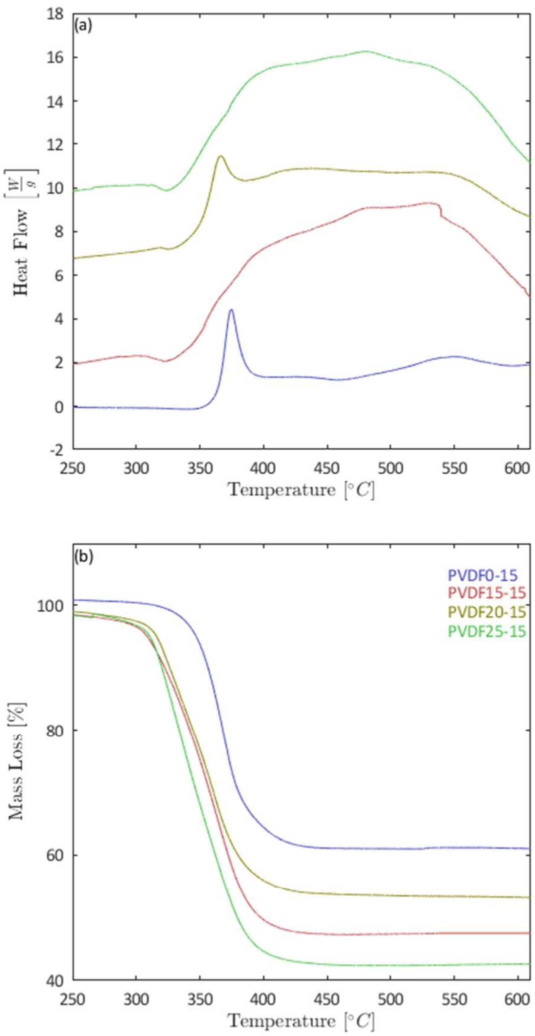

Figure 2 - Heat flow (a) and mass loss (b) for blends with 15 wt% nAl.

Generally, PMMA and PVDF are highly miscible at low PVDF loadings. However, at PVDF loadings greater than 50 wt%, the phase domains separate into PVDF crystallites, an amorphous PVDF/PMMA region and an amorphous-crystalline interface. The glass transition temperatures for virgin PVDF and PMMA are approximately -35 °C and 100 °C, respectively. Primary nucleation will occur around the PVDF crystallization temperature (i.e., ≈ 140 °C). Upon cooling, chain mobility in the PMMA chains will decrease significantly once temperatures drop below the glass transition temperature.

This will effectively decrease the PVDF crystal growth rates by limiting the transport contributions to PVDF nucleation because chains must diffuse through the rigid PMMA network in order to reach the crystal front. Although the PMMA glass transition is lowered in PVDF/PMMA blends, this limitation is present nonetheless. Generally, crystal growth rates in completely miscible polymer blends decrease significantly when one of the polymers has a high glass transition temperature. This effect has been observed in polyethylene oxide/poly(styrene-*co*-hydroxystyrene) blends.[34] However, if the temperature can be maintained and controlled between the PMMA glass transition and the PVDF melt temperatures, diffusion coefficients may be optimized and higher crystallinities may be reached.

The addition of Al particles decreases PVDF diffusion through electrostatic interactions with Al particles, subsequently reducing chain motion. This effect is evident in PVDF0-YY samples as Al concentration ranges from 0 to 30 wt%. Increasing particle surface area results in stronger electrostatic interactions between Al particle surface and the CF dipole in PVDF. With increasing PMMA concentration, this effect is reduced as particles begin to interact with the carbonyl group in PMMA resulting in an overall increase in PVDF crystallinity (see Table 3).[29]

Decomposition onset temperature (T_d) for the blends decrease in a step-wise fashion with both increasing PMMA and Al concentration in PVDF compared with virgin PVDF (see Figure S3). In PVDFXX-0 blends, this decrease is attributed to the decomposition of PMMA prior to the onset of PVDF decomposition (see Table 3). The decomposition of PMMA prior to PVDF decomposition creates voids in the composite, which result in a reduction of PVDF thermal stability. A similar trend is observed in nAl loaded samples.

In the nAl-loaded samples, there are three decomposition mechanisms at play. With increasing temperature, (1) PMMA begins to decompose, followed by (2) accelerated PVDF decomposition due to interactions with the Al_2O_3 monolayer,[5,16] and finally (3) pyrolysis of any remaining PVDF.[5] At higher Al loadings, the nanoparticles have a large aspect ratio, which enhances formation of bridges between them, known as conductive networks.[35] The conductive networks work to facilitate heat distribution in the sample and as a result, PMMA decomposes at a lower temperature. However, this study showed first decomposition temperature, $T_{d,1}$, slightly increases or is stabilized as the PMMA loading increases which can be attributed to the carbonyl group of PMMA interacting with the Al oxide surface instead of the CH_2 group of PVDF. Thermal stability of PMMA is enhanced through this interaction. Li et al. observed the same trends in the PVDF/PMMA and PVDF/PMMA/TiO_2 blends.[8] If any PVDF remains at higher temperatures, it]decomposed through pyrolysis to carbonaceous char.[5] The decomposition onset will continue to decrease with further addition of nAl, eventually eliminating PVDF decomposition through pyrolysis at higher temperatures.

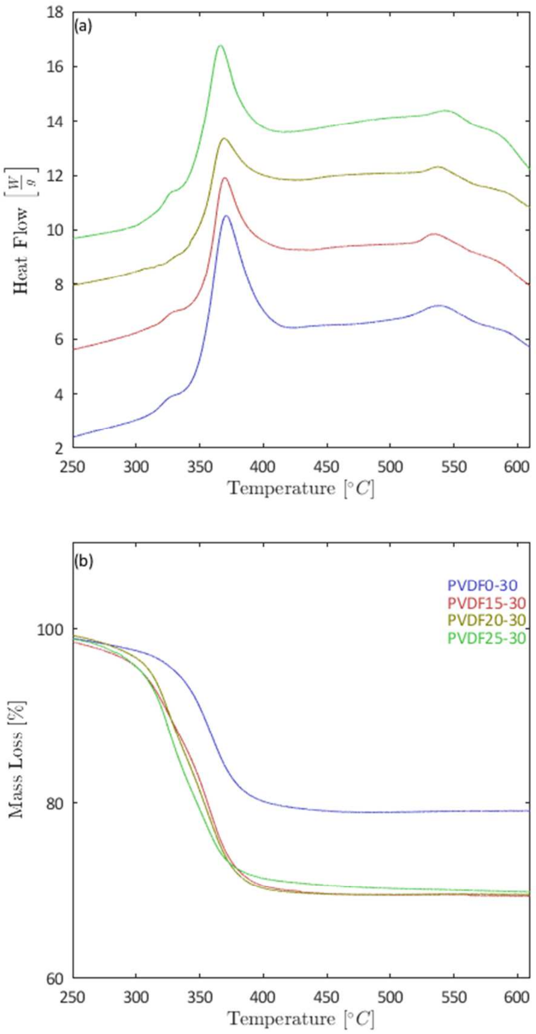

Figure 3 - Heat flow (a) and mass loss (b) for blends with 30 wt% nAl.

Table 3 - SDT analysis for each blend, including melt temperature (T_m), melt enthalpies (ΔH_m), degree of crystallinity (X_c), decomposition event temperature (T_d), and char yield percentage.

		Melt			**Decomposition**	
	T_m *[°C]*	**ΔH_m** *[J/g]*	**X_c** *[%]*	**$T_{d,1}$** *[°C]*	**$T_{d,2}$** *[°C]*	**Char Yield** *[%]*
PVDF0-0	161	51	49	–	434	32
PVDF15-0	159	38	42	368	426	30
PVDF20-0	158	34	40	372	426	27
PVDF25-0	157	30	38	368	426	28
PVDF100-0	–	–	–	360	–	<1
PVDF0-15	162	29	28	–	369	61
PVDF15-15	159	28	32	320	366	51
PVDF20-15	158	28	33	326	361	53
PVDF25-15	157	27	34	331	363	42
PVDF0-30	159	24	23	–	359	79
PVDF15-30	158	24	27	322	357	69
PVDF20-30	157	22	27	325	357	69
PVDF25-30	157	20	25	326	358	56

Char yield results are insightful for each composite. Virgin PVDF and PMMA samples produce char yields of 32 and 0.5 wt%, respectively. The PVDF/PMMA blends (i.e., PVDFXX-0) produce char yields from TGA close to that of the calculated weighted averages of the virgin filaments (i.e., < 5 wt% deviation). This suggests that PVDF char yield is not affected by the presence of PMMA. In Al-loaded samples (i.e., PVDFXX-15 and PVDFXX-30), char yield trends deviate from that of their weighted averages. Specifically, PVDF0-15 produces a char yield of 61 wt%, which is 13 wt% higher than the weighted average. This trend continues in PVDF0-30 with a 22 wt% deviation from the weighted average. As mentioned above, PVDF decomposition is accelerated by the Al_2O_3 monolayer on the surface of the Al particles. As PVDF decomposes, it releases HF gas, which then reacts with Al to produce AlF_3. As Al concentration increases, the number of reaction sites increase through more available surface area. The deviation from weighted averages is due to this HF reaction with Al_2O_3. According to the char yield results, HF reaction decreases with PMMA loading. This deviation decreases from 13 wt% to nearly 0 wt% in PVDF0-15 and PVDF25-15, respectively. Similarly, PVDF0-30 and PVDF25-30 samples exhibit a decrease in available HF from 22 to 12 wt%. In an equilibrium setting, PMMA decomposition onset occurs before PVDF decomposition onset, which leads to HF reacting to the Al oxide layer. This results in convective pathways that once contained PMMA, which allows an additional pathway for HF escape. Figures 2 and 3 show the heat flow and mass loss curves from SDT analysis for PVDF/PMMA blends with 15 wt% nAl and 30 wt% nAl, respectively. The endothermic event with peaks between 155 and 162°C for all specimens indicates the PVDF melt (see Figure S4). Table 3 shows that the decomposition temperature has a decreasing trend as Al content increases. From SDT analysis, the lowest observed decomposition onset temperature is 296 °C and the lowest observed melt temperature is 157 °C. This allows a range of 139 °C to explore optimum processing and printing temperatures by investigating melt flow rates or viscosity at any temperature between the lowest melt temperature and lowest decomposition temperature.

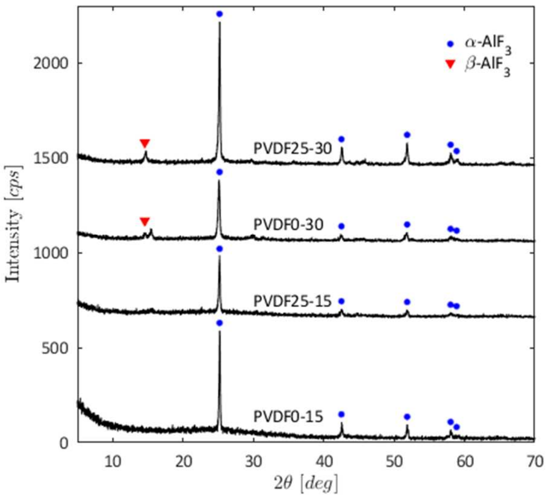

Figure 4 - XRD spectra for pure PVDF and 25 wt% PMMA composites loaded with 15 wt% and 30 wt% nAl.

Combustion Performance

Figure 4 shows XRD profiles for burn products of 15 wt% and 30 wt% composites. In each spectrum, the only peaks

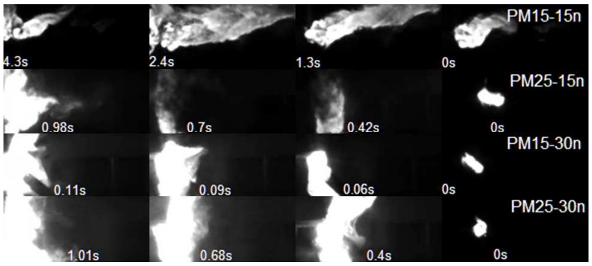

Figure 5 - Ignition still frames for PVDF15-15, PVDF25-15, PVDF15-30, and PVDF25-30.

identified were those representative of α-AlF_3. This indicates that during the burn, PMMA does not participate in the reaction between Al and PVDF. Instead, high loadings of PMMA may serve as a heat sink which slows the burn rate. This is consistent with findings from burn rate studies shown below.

Table 4 - Burn rates calculated with MATLAB.

Sample	Average Burn Rate [cm/sec]	Equivalence Ratio (ϕ)
PVDF0-15	2.0	0.47
PVDF15-15	2.4	0.56
PVDF25-15	4.4	0.63
PVDF0-30	13.0	1.2
PVDF15-30	8.3	1.4
PVDF25-30	4.1	1.5

Interestingly, this burn performance is only observed in melt-processed blends. McCollum et al. discovered the same α-AlF_3 burn products from injection molded Al/PVDF coupons when burned in air.[5] However, Zachariah and colleagues found that AlF_3 formation in open air burns is hindered in electrosprayed films at similar loadings.[3] When burned in air, the electrosprayed composites yielded Al_2O_3 and Al_4C_3, but no AlF_3. When these blends were burned in an inert environment, AlF_3 was the dominant reaction product. This implies that the condensed composites produced via melt-processing techniques are a more efficient means for AlF_3 formation. The cost, however, is that the reaction temperature is likely lower for melt-processed composites opposed to their solution-processed counterparts. More work needs to be done to resolve this phenomenon.

The combustion propagation velocity of the samples was measured from 3D printed specimens by igniting with a propane torch. The flame front was tracked as a function of time using a custom MATLAB function. The MATLAB function takes the high-speed video as an input. A still frame was taken as a reference to convert the raw data to cm/sec. Samples were easily ignited and showed consistent, self-sustaining, and steady flame propagation. Representative flame propagation is shown in Figure 5 for four different samples. The average burn rates for each sample are summarized in Table 4.

Zachariah et al. reported flame speeds of 5 cm/s in electrosprayed Al/PVDF films with Al loadings of 16.7 wt% in open air.[3] The key difference here is that the relatively porous morphologies do not retain HF or prevent oxygen permeation resulting in a competitive reaction mechanism. Further increasing Al concentrations to 50 wt% Al results in flame speeds up to 23 cm/s.[3] Due to the competitive reaction mechanism (formation of Al_4C_3 and AlF_3), a stoichiometric blend is likely to occur at higher Al concentrations. Although the reaction mechanism varies for Al-PTFE blends, high surface area powder blends produce flame speeds that can exceed 5 m/s.[36]

The reaction mechanism for Al/PVDF blends initiates with the accelerated decomposition of PVDF, resulting in HF gas evolution. The HF gas reacts with the Al_2O_3 shell forming AlF_3. Because the nano-scale Al has high surface area, this process is the primary decomposition mechanism for the blends studied here. As shown from XRD, reaction products are independent of PMMA concentration. This means that the Al/PVDF reaction mechanism is not significantly altered by the presence of PMMA. Because Al content was constant in all PVDFXX-15 and PVDFXX-30 samples, the composite stoichiometry increased with PMMA content. Consider the reaction mechanism proposed by Zachariah and coworkers.[16]

$$Al_2O_3 + (C_2H_2F_2)_n \rightarrow \left(C_xH_yF_z\right) + HF_{(g)} \tag{4}$$

$$(C_2H_2F_2)_n \rightarrow \left(C_xH_yF_z\right) + HF_{(g)} + C \tag{5}$$

$$\left(C_xH_yF_z\right) \rightarrow HF_{(g)} + C \tag{6}$$

$$2Al + 6\mathrm{HF} \rightarrow 2AlF_3 + 3H_{2\mathrm{(g)}} \tag{7}$$

Here, equation (4) represents accelerated PVDF decomposition from reactions with Al_2O_3. Remaining PVDF will decompose by pyrolysis (see equation (5)). Next, PVDF intermediates reduce to form HF gas and C char (see equation (6)). Finally, the exothermic reaction occurs when Al reacts with the evolved HF gas, forming AlF_3 and expelling H_2 gas (equation (7)).

One important phenomena to note is the lack of Al_2O_3 peaks in post-burn XRD spectra. In the study carried out by Zachariah and co-workers, Al_2O_3 was defined as a catalyst because it remained unchanged during the reaction.[16] This was found by performing XRD on films in pre and post-burn conditions. Here, Al_2O_3 acts as a co-reactant as no trace Al_2O_3 peaks were discovered in post-burn XRD spectra. The likely cause is that HF reacts with Al in the Al_2O_3 lattice and releases oxygenated species. Further studies must be performed to identify any oxygen-containing species (e.g., O_2, CO_2, etc.) evolved during decomposition.

Burn rate behavior can be explained in part by changes in thermal diffusivity with composition. Specifically, the thermal diffusivity of PVDF/PMMA blends increases with PMMA loading, which leads to more efficient conductive heat transfer in the condensed samples.[37] This effect is seen in fuel lean samples as burn rates increase from 2.0 to 4.4 cm/s for 0 and 25 wt% PMMA, respectively. However, flame speeds decreased with increasing PMMA concentration in the PVDFXX-30 (i.e., fuel rich) blends as some of the energy generated from the energetic reaction was used to decompose PMMA, which indicates that heat transfer efficiency is only part of the solution. X-ray diffraction of the post-burn char indicates that PMMA has little impact on solid products formed during sample burns. In all cases, α-AlF_3 and amorphous carbon char were the only two condensed products identified. This implies that PMMA does not significantly contribute to the Al-PVDF reaction.

By considering only the weight fractions of Al and PVDF in each sample, equivalence ratios show an increase in stoichiometry as PMMA loading increases. In fuel-rich samples, the decrease in burn rate can be attributed to an increase in stoichiometry beyond that of an ideal blend (i.e., ϕ=1). This means that stoichiometry can be tuned through PMMA addition without sacrificing processability. Using Equation 4, a stoichiometric blend occurs with Al and PVDF concentrations of 27 wt% and 73 wt%, respectively. This finding provides an opportunity to tune burn behavior in blends by varying PMMA concentration without altering the reaction mechanism or sacrificing processability.

Conclusions

Fluorinated energetic composites were fabricated via fused deposition modeling with varying concentrations of PMMA. Increasing PMMA concentrations enhanced β-phase PVDF formation in composites regardless of Al loading. In order to increase β-phase content, two approaches may yield favorable results. First, to reduce electrostatic interactions between Al particles and the CF dipole, particle functionalization may provide additional primary nucleation sites for β-phase crystal growth. Secondly, in both extrusion and printing processes, more precise temperature control may improve crystal formation by slowing the cooling rate between the nozzle and build plate thus enhancing continuity in the electroactive phase for sensing and actuating functionality. Faster cooling rates are detrimental to the diffusion of PVDF chains to a growing crystal front. Both approaches will be covered in more detail in future work. This work leads the way for tunable energetics, specifically, 3D printing piezoelectric energetic composites. Although decomposition temperatures decreased when increasing both PMMA and Al concentrations, the overall reaction mechanism remained unchanged. X-ray diffraction of burn products revealed that the primary solid product in each burn was α-AlF_3. This finding suggests that the condensed composites produced via melt processing allow for a more efficient reaction between Al and PVDF. Finally, burn rates increased in fuel lean samples, but decreased in fuel rich samples with increasing PMMA concentration. This is due to changes in composite stoichiometry, which is optimized in PVDF0-30 samples (i.e., closest to stoichiometric). This finding may allow for controlled burn rates without sacrificing burn efficiency.

Conflicts of interest

There are no conflicts to declare.

Acknowledgements

Authors thank Dr. Geoff McHarg (Space Physics and Atmospheric Research Center (SPARC), United States Air Force Academy) for the high-speed camera in order to determine burn rates. This work was supported by the Air Force Office of Scientific Research. Additional support was provided by the Air Force Research Laboratory, Munitions Directorate, Eglin Air Force Base, FL. J.M. and J.A.B. were supported by the Air Force Research Laboratory Summer Faculty Fellowship Program.

References

1 A. C. Balazs, T. Emrick and T. P. Russell, *Science (80-.).*, 2006, **314**, 1107–1110.
2 F. D. Ruz-Nuglo and L. J. Groven, *Adv. Eng. Mater.*, 2017, **1700390**, 1–8.
3 C. Huang, G. Jian, J. B. DeLisio, H. Wang and M. R. Zachariah, *Adv. Eng. Mater.*, 2014, **17**, 95–101.
4 T. J. Fleck, A. K. Murray, I. E. Gunduz, S. F. Son, G. T. C. Chiu and J. F. Rhoads, *Addit. Manuf.*, 2017, **17**, 176–182.
5 J. McCollum, A. M. Morey and S. T. Iacono, *Mater. Des.*, 2017, **134**, 64–70.
6 W. Ma, J. Zhang and X. Wang, *Appl. Surf. Sci.*, 2008, **254**, 2947–2954.
7 S. Schneider, X. Drujon, J. C. Wittmann and B. Lotz, *Polymer (Guildf).*, 2001, **42**, 8799–8806.
8 W. Li, H. Li and Y. M. Zhang, *J. Mater. Sci.*, 2009, **44**, 2977–2984.
9 E. Freire, O. Bianchi, E. E. C. Monteiro, R. C. Reis Nunes and M. C. Forte, *Mater. Sci. Eng. C*, 2009, **29**, 657–661.
10 P. Martins, A. C. Lopes and S. Lanceros-Mendez, *Prog. Polym. Sci.*, 2014, **39**, 683–706.
11 F.-C. Chiu, C. C. Chen and Y.-J. Chen, *J. Polym. Res.*, 2014, **21**, 378.
12 Kap Jin Kim, Yong Ju Cho and Young Ho Kim, *Vib. Spectrosc.*, 1995, **9**, 147–159.
13 R. Gregorio Jr and Nadia Chaves Pereira de Souza Nociti, *J. Phys. D Appl. Phys*, 1995, **28**, 432–436.
14 R. Sengupta, S. Chakraborty, S. Bandyopadhyay, S. Dasgupta, R. Mukhopadhyay, K. Auddy and a S. Deuri, *Polym. Eng. Sci.*, 2007, **47**, 21–25.
15 B. R. Hahn, O. Herrmann-Schönherr and J. H. Wendorff, *Polymer (Guildf).*, 1987, **28**, 201–208.
16 J. B. Delisio, X. Hu, T. Wu, G. C. Egan, G. Young and M. R. Zachariah, *J. Phys. Chem. B*, 2016, **120**, 5534–5542.
17 S. Chaturvedi and P. N. Dave, *Arab. J. Chem.*, 2013.
18 D. W. Kim, K. T. Kim, T. S. Min, K. J. Kim and S. H. Kim, *Sci. Rep.*, 2017, **7**, 4659.
19 L. Galfetti, L. T. De Luca, F. Severini, L. Meda, G. Marra, M. Marchetti, M. Regi and S. Bellucci, *J. Phys. Condens. Matter*, 2006, **18**, S1991–S2005.
20 J. B. Delisio, C. Huang, G. Jian, M. R. Zachariah and G. Young, in *American Institute of Aeronautics and Astronautics*, 2014, pp. 1–8.
21 C. A. Crouse, C. J. Pierce and J. E. Spowart, *Combust. Flame*, 2012, **159**, 3199–3207.

22 D. S. Sundaram, V. Yang and V. E. Zarko, *Combust. Explos. Shock Waves*, 2015, **51**, 173–196.

23 C. A. Crouse, C. J. Pierce and J. E. Spowart, *Polym. Prepr.*, 2011, **52**, 742–743.

24 W.-K. Lee and C.-S. Ha, *Polymer (Guildf).*, 1998, **39**, 7131–7134.

25 I. S. Elashmawi and N. A. Hakeem, *Polym. Eng. Sci.*, 2008, **48**, 895–901.

26 X. Zhao, S. Chen, J. Zhang, W. Zhang and X. Wang, *J. Cryst. Growth*, 2011, **328**, 74–80.

27 H. Sasaki, P. Kanti Bala, H. Yoshida and E. Ito, *Polymer (Guildf).*, 1995, **36**, 4805–4810.

28 E. Freire, O. Bianchi, J. N. Martins, E. E. C. Monteiro and M. M. C. Forte, *J. Non. Cryst. Solids*, 2012, **358**, 2674–2681.

29 S. Pletincx, K. Marcoen, L. Trotochaud, L.-L. Fockaert, J. M. C. Mol, A. R. Head, O. Karslioğlu, H. Bluhm, H. Terryn and T. Hauffman, *Sci. Rep.*, 2017, **7**, 13341.

30 J. Arranz-Andrés, N. Pulido-González, C. Fonseca, E. Pérez and M. L. Cerrada, *Mater. Chem. Phys.*, 2013, **142**, 469–478.

31 M. Lee, T. Koo, S. Lee, B. H. Min and J. H. Kim, *Polym. Compos.*, 2015, **36**, 1195–1204.

32 L. Wang and S. Chen, *J. Therm. Anal. Calorim.*, 2016, **125**, 215–230.

33 B. Crist and J. M. Schultz, *Prog. Polym. Sci.*, 2016, **56**, 1–63.

34 J. K. Hobbs, T. J. Mcmaster, M. J. Miles and P. J. Barham, *Polymer (Guildf).*, 1998, **39**, 586–7.

35 G.-W. Lee, M. Park, J. Kim, J. I. Lee and H. G. Yoon, *Compos. Part A Appl. Sci. Manuf.*, 2006, **37**, 727–734.

36 K. W. Watson, M. L. Pantoya and V. I. Levitas, *Combust. Flame*, 2008, **155**, 619–634.

37 N. Tsutsumi, M. Terao and T. Kiyotsukuri, *Polymer (Guildf).*, 1993, **34**, 90–94.